

Helicity generation and subcritical behaviour in rapidly rotating dynamos

Binod Sreenivasan¹ and Chris A. Jones^{2†}

¹ Department of Mechanical Engineering, Indian Institute of Technology, Kanpur 208016, India

² Department of Applied Mathematics, University of Leeds, Leeds LS2 9JT, UK

(Received 6 August 2010; revised 5 April 2011; accepted 16 May 2011;
first published online 19 August 2011)

Numerical dynamo models based on convection-driven flow in a rapidly rotating spherical shell frequently give rise to strong, stable, dipolar magnetic fields. Dipolar dynamos can be subcritical in the sense that strong magnetic fields are sustained at a Rayleigh number lower than that required for a dynamo to grow from a small seed field. In this paper we find subcritical behaviour in dynamos in line with previous studies. We explore the action of Lorentz force in a rotating dynamo which gives rise to a strong preference for dipolar modes over quadrupolar modes, and also makes subcritical behaviour more likely to occur. The coherent structures that arise in rapidly rotating convection are affected by the magnetic field in ways which strongly increase their helicity, particularly if the magnetic field is dipolar. As helicity enhances dynamo action, an existing magnetic field can hold itself up, which leads to subcritical behaviour in the dynamo. We investigate this mechanism by means of the asymptotic small Ekman number theory of rapidly rotating magnetoconvection, and compare our results with fully nonlinear dynamo simulations. There are also other mechanisms which can promote subcritical behaviour. When Reynolds stresses are significant, zonal flows can lower the helicity and disrupt the onset of dynamo action, but an established dipole field can suppress the zonal flow, and hence boost the helicity. Subcriticality means that a slow gradual reduction in Rayleigh number can lead to a catastrophic collapse of the dynamo once a critical Rayleigh number is reached. While there is little evidence that the Earth is currently in a subcritical regime, this may have implications for the long-term evolution of the geodynamo.

Key words: dynamo theory, geodynamo, magnetoconvection

1. Introduction

Planetary magnetic fields are generated by dynamo action occurring in their cores. The electrical conductivity arises either from the presence of a liquid iron core, or in the case of giant planets from metallic hydrogen present due to high pressure in the deep interior. It is widely believed that the fluid in planetary cores is stirred by the convection which transports the heat outward from the deep interior, though precessional effects may also be involved in magnetic field production. There has been considerable progress in modelling convection in rapidly rotating fluid shells, and the way in which it may lead to dynamo action; see for example the recent reviews of Kono & Roberts (2002) and Christensen & Wicht (2007). The case of Boussinesq

† Email address for correspondence: C.A.Jones@maths.leeds.ac.uk, bsreeni@iitk.ac.in

convection, where the only density variations allowed are the small fluctuations driving the flow, has been particularly well studied. There are, however, numerical difficulties in reaching the rather extreme values of the parameters found in planetary cores, in particular the very low Ekman number, E , and magnetic Prandtl number ν/η , where ν is the kinematic viscosity and η is the magnetic diffusivity.

These studies of convection-driven dynamos have revealed that many different types of magnetic field may be generated, for example axial dipoles, quadrupoles (see e.g. Busse & Simitev 2006) and even equatorial dipoles (Aubert & Wicht 2004), that is, a dipolar field with its axis lying in the equatorial plane. However, there is a large region of the parameter space where axial dipole dynamos dominate, which is essentially where the inertial terms in the equation of motion are negligible, that is, at very low Rossby number (Sreenivasan & Jones 2006a). Simple estimates of the core flow velocity (see e.g. Jones 2007) suggest that inertia will only be significant in planetary cores at length scales so small that magnetic diffusion is very rapid, so the expected regime is indeed where axial dipole dominance is found. This may explain why most planetary dynamos are approximately axial dipoles, the only exceptions being Uranus and Neptune, whose physical properties are poorly understood.

While the dipole dominance of low-Rossby-number spherical-shell convection-driven dynamos is well known, its physical reasons are not well understood. Convection in rapidly rotating spherical geometry takes the form of columns parallel to the rotation axis (Roberts 1968; Busse 1970; Zhang 1992) and this is also observed in experiments (Busse & Carrigan 1976). However, this flow in itself does not necessarily lead to an axial dipole dynamo. Taking z as the coordinate parallel to the rotation axis, if the rolls have no flow component in the z direction there can be no dynamo as the flow is then planar (Zeldovich 1957). In the Roberts (1970) flow $\mathbf{u} = (\cos y, \sin x, \sin y + \cos x)$ in Cartesian geometry, where there is flow parallel to z along the rolls, a magnetic field can be generated, but it is aligned perpendicular to the rolls, and not parallel to them. Cardin & Schaeffer (2006) investigated dynamo action in spherical geometry produced by rolls whose axis was in the z direction but which also had a flow component parallel to z with u_z proportional to z . This flow has the same equatorial symmetry as convection-driven flow in rotating spherical geometry, but nevertheless, Cardin and Schaeffer found that quadrupolar modes were generally preferred over axial dipolar modes. The preference for axial dipoles in convection-driven dynamos is not simply a matter of having columnar convection together with a u_z of the right equatorial symmetry. We explore below why axial dipolar modes are common in convection-driven, rotating-dynamo simulations.

Another feature of convection-driven dynamos is that they can show subcritical behaviour. This means that the bifurcation from non-magnetic, nonlinear rotating convection to a magnetic state can be subcritical. Note that this is a slightly different issue from the distinction between a strong-field and a weak-field dynamo that was discussed by Roberts & Soward (1992). The scenario we discuss here relates to figure 3 of that paper, whereas in the strong-field dynamo picture, it is suggested that because the magnetic field can increase the thickness of the convection rolls, it might be possible to find a nonlinear convecting magnetic state at a Rayleigh number below that required for the onset of non-magnetic convection (Fautrelle & Childress 1982). This may indeed be possible, but in this paper, although we find fully nonlinear magnetic solutions below the critical Rayleigh number for the onset of dynamo action from a small seed field, we never found such fully nonlinear states at the much lower Rayleigh numbers at which convection itself sets in.

The existence of subcriticality in the sense that nonlinear magnetic solutions can exist at Rayleigh numbers below that required for the onset of dynamo action from a small seed field might be inferred from the fact that the dynamo benchmark (Christensen *et al.* 2001) can be found if the specified (strong) magnetic field is used as an initial condition, but it cannot be found at the given parameters by starting from a random seed magnetic field. Perhaps surprisingly, there have not been many investigations of subcritical behaviour in spherical dynamo simulations, though a recent exception is Morin & Dormy (2009).

In the nonlinear numerical simulations, it is not always a simple matter to understand which interactions are important for a particular physical effect, such as the existence of subcriticality. We have therefore also investigated the problem of the onset of convection with an imposed magnetic field, which is amenable to asymptotic analysis in the relevant low- E limit (Jones, Mussa & Worland 2003). This enables us to investigate how the flow is affected by the magnetic field, which is relevant to the issue of subcriticality because it is when the flow changes in a way which enhances dynamo action that we may expect subcritical behaviour. A similar approach was adopted by Busse (1976) in the context of the annulus model of rapidly rotating convection (see e.g. Busse 1970). In the work of Jones *et al.* (2003), attention was focused (for computational reasons) on the case of the Malkus field, $B_\phi = B_0 s$, where s is the distance from the rotation axis. This field has quadrupolar symmetry, and the main effect found was the thickening of the convection columns with increasing field strength. Below we also focus on the differences in the flow patterns induced by dipolar and quadrupolar fields.

To estimate whether a particular flow pattern enhances dynamo action or not we compare the helicity generated by different flows. It is known that helicity is not essential for dynamo action but it helps (Gilbert, Frisch & Pouquet 1988), and the critical magnetic Reynolds numbers for flows with helicity are generally lower than those without helicity (e.g. Roberts 1970). The analysis of the dynamo mechanism operating in spherical convection-driven dynamos (Olson, Christensen & Glatzmaier 1999) also suggested that helical flow was important in generating the field. Recent studies with laterally varying thermal boundary conditions (Sreenivasan 2009) suggest that the helicity produced by inhomogeneities at the Earth's core-mantle boundary (CMB) can, under negligible background convection, support the long-time, high-latitude flux lobes in the observed geomagnetic field. Here the lateral variations at the boundary drive strong axial fluid motions via the Coriolis force, in turn generating the helicity that amplifies a seed magnetic field. All of the above studies have provided the impetus to understand the role of helicity in field generation in rapidly rotating dynamos.

The geodynamo is probably strongly supercritical at the present time, and so its effective Rayleigh number is well above the relatively near-critical values investigated here. However, the compositional and thermal driving of the geodynamo is likely to continually diminish over geological time as the Earth cools, and any radioactive heat sources will also gradually weaken. So if the geodynamo goes into a subcritical state, it may suffer a sudden death rather than a slow extinction. There is evidence that Mars had a strong field in the past, but that the field collapsed some 350 myr after the planet's formation (Lillis *et al.* 2008). There are several possible explanations for this, but Kuang, Jiang & Wang (2008) have suggested that if the Martian dynamo was in a subcritical state, this might have led to a sudden collapse rather than a more gradual decline.

2. Governing equations

We consider a thermal convection-driven dynamo where an electrically conducting fluid is confined between two concentric, co-rotating spherical surfaces. The radius ratio r_i/r_o is chosen to be that in the Earth, 0.35. In the Boussinesq approximation, the time-dependent, 3-D magnetohydrodynamic equations for the velocity \mathbf{u} , the magnetic field \mathbf{B} and the temperature T are solved. The governing dimensionless equations are

$$\begin{aligned} \frac{E}{Pm} \left(\frac{\partial \mathbf{u}}{\partial t} + (\nabla \times \mathbf{u}) \times \mathbf{u} \right) + 2\hat{\mathbf{z}} \times \mathbf{u} \\ = -\nabla p^* + Ra \frac{Pm}{Pr} T \frac{\mathbf{r}}{r_o} + (\nabla \times \mathbf{B}) \times \mathbf{B} + E \nabla^2 \mathbf{u}, \end{aligned} \quad (2.1)$$

$$\frac{\partial \mathbf{B}}{\partial t} = \nabla \times (\mathbf{u} \times \mathbf{B}) + \nabla^2 \mathbf{B}, \quad (2.2)$$

$$\frac{\partial T}{\partial t} + (\mathbf{u} \cdot \nabla) T = Pm Pr^{-1} \nabla^2 T, \quad (2.3)$$

$$\nabla \cdot \mathbf{u} = 0, \quad (2.4)$$

$$\nabla \cdot \mathbf{B} = 0, \quad (2.5)$$

where p^* is an augmented fluid pressure that includes the irrotational part of the nonlinear inertial forces. The dimensionless groups in (2.1), (2.2), (2.3) are the Ekman number, $E = \nu / \Omega L^2$, the Prandtl number, $Pr = \nu / \kappa$, the magnetic Prandtl number, $Pm = \nu / \eta$ and the ‘modified’ Rayleigh number $Ra = g_o \alpha \Delta T L / \Omega \kappa$. In the above dimensionless groups, ν is the kinematic viscosity, κ is the thermal diffusivity, η is the magnetic diffusivity, L is the gap width of the spherical shell, Ω is the angular velocity of rotation, g_o is the gravitational acceleration at the upper boundary, α is the coefficient of thermal expansion and ΔT is the superadiabatic temperature difference between the boundaries. The Ekman number is a measure of the rotation rate and the Rayleigh number represents the strength of convective buoyancy in the problem. As velocity is scaled by η / L , the volume-averaged dimensionless velocity in the model directly gives the magnetic Reynolds number, R_m . The unit of magnetic field is $(\Omega \rho \eta \mu)^{1/2}$, and the unit of time is L^2 / η . Both stress-free and no-slip boundary conditions are investigated. The two boundaries are kept electrically insulating and isothermal. The applied basic state temperature distribution is one of pure basal heating, $T_0(r) = \beta / r$, where $\beta = r_i r_o$.

Note that when stress-free boundary conditions are used in conjunction with insulating boundaries, the total angular momentum of the core fluid is conserved. The angular momentum value must therefore be set in the initial condition, and the natural choice, which we made here, is that the total angular momentum is exactly that of uniformly rotating fluid with angular velocity Ω . This means the angular momentum relative to the rotating mantle frame is zero. Some care must be taken here, because if initial conditions from no-slip solutions are used, the relative angular momentum will not in general be zero.

The system equations are solved using a pseudospectral method in which the magnetic field and the velocity are expanded as toroidal and poloidal scalars (broadly similar to the method described in Clune *et al.* 1999), for example the magnetic field \mathbf{B} is written

$$\mathbf{B} = \nabla \times \mathcal{T} \mathbf{r} + \nabla \times \nabla \times \mathcal{P} \mathbf{r}. \quad (2.6)$$

The scalars \mathcal{T} and \mathcal{P} are then expanded in spherical harmonics, and the numerical equations are derived from the coefficients in these expansions.

3. The dynamo properties of linear magnetoconvection at low Ekman number

Busse developed the annulus model (Busse 1970) (see also Jones 2007 for a recent review) to explore convection in rapidly rotating fluids. He then used the linear theory of magnetoconvection in rotating systems to explore the onset of dynamo action (Busse 1976) using the annulus model. He found the surprising result that the effect of a magnetic field on convection can enhance magnetic field generation. This suggests that it could lead to subcritical behaviour. Here we use the asymptotic theory of convection in a rotating spherical shell in the limit $E \rightarrow 0$ to explore this idea further.

The asymptotic theory of the onset of rapidly rotating convection in the low- E limit was originated by Roberts (1968) and Busse (1970), and developed by Jones, Soward & Mussa (2000) and Dormy *et al.* (2004). In the configuration used here, the heating is differential, that is, all the heat flux enters the bottom boundary, and there is no internal heating. In this situation, Dormy *et al.* (2004) showed that the onset of convection occurs close to the tangent cylinder (an imaginary cylinder touching the inner boundary and parallel to the axis). They also noted that this situation is a little simpler than the case where the heating is internal and the onset of convection occurs at some point in the interior of the fluid (Jones *et al.* 2000). When the onset occurs at the inner core boundary, the solution has three different length scales in the cylindrical polar coordinate s , ϕ and z directions,

$$\frac{1}{s} \frac{\partial}{\partial \phi} \sim O(E^{-1/3}), \quad \frac{\partial}{\partial s} \sim O(E^{-2/9}), \quad \frac{\partial}{\partial z} = O(1) \quad \text{as } E \rightarrow 0. \quad (3.1)$$

The weak z -dependence means that the velocity can be written in a quasigeostrophic form,

$$\mathbf{u} = u_z \hat{\mathbf{z}} + \nabla \times \psi \hat{\mathbf{z}}. \quad (3.2)$$

The boundary conditions require that u_z and u_s are the same order of magnitude in the $E \rightarrow 0$ limit, but u_ϕ is $O(E^{1/9})$ smaller. This is because in the asymptotic limit $E \rightarrow 0$, the radial wavenumber scales as $O(E^{-2/9})$ whereas the azimuthal wavenumber scales as $O(E^{-1/3})$ (Dormy *et al.* 2004), so the spiralling angle of the convection pattern becomes small. This vanishing of the spiralling angle is specific to the case where onset occurs near the tangent cylinder. When these scalings are inserted into the equations, a Wentzel–Kramers–Brillouin (WKB) theory emerges, in which the z -structure is determined by a second-order equation known as the Roberts–Busse equation and the s -dependence is governed by an Airy equation (see (3.18) of Dormy *et al.* 2004). Disturbances have dependence $\exp(im\phi - i\omega t)$, where $m \sim E^{-1/3}$ and $\omega \sim E^{-2/3}$, so we replace ψ by the real part of $A(s)\psi(z)\exp(im\phi - i\omega t)$ and u_z by the real part of $A(s)u_z(z)\exp(im\phi - i\omega t)$, where the amplitude function $A(s)$ is an Airy function (see Dormy *et al.* 2004 for details). This second order system is affected by the magnetic field, but provided the field is not too strong the scalings (3.1) remain the same (Jones *et al.* 2003). In the induction equation, field is generated by the $\mathbf{B} \cdot \nabla \mathbf{u}$ term. Because the shortest length scale is in the ϕ direction, the ϕ -component of magnetic field has the strongest influence on the convection, provided all three magnetic field components have a similar field strength, which our nonlinear simulations suggest is true. We can therefore simplify the problem significantly by considering only an azimuthal field in the magnetoconvection problem.

Using equations (3.14)–(3.18) of Jones *et al.* (2003) (modified slightly to take into account the different non-dimensional units), the linearised z -vorticity equation is then

$$E(a^2 - i\omega Pm^{-1})a^2\psi - 2\frac{du_z}{dz} + \frac{imRaPm}{Pr r_o}\theta = -\Lambda\left(\frac{b_\phi}{s}\right)^2 \frac{m^2 a^2}{a^2 - i\omega}\psi \quad (3.3)$$

where ω is the frequency, ψ the horizontal flow streamfunction, u_z is z -velocity, θ is temperature perturbation, $a^2 = k^2 + m^2/s^2$, k being the radial wavenumber, and $k=0$ when onset of convection occurs close to the tangent cylinder as here. The magnetic field B_ϕ is written as B_0 times a normalised b_ϕ , and the Elsasser number $\Lambda = B_0^2/\Omega\rho\mu\eta$. In this equation, the z -vorticity $\zeta_z = a^2\psi$ is driven by the buoyancy, damped by the magnetic field (though damping is reduced if m reduces), further damped by viscosity and moderated by stretching of the vorticity due to the background rotation.

The equations for the z -velocity and temperature perturbation complete the system

$$E(a^2 - i\omega Pm^{-1})u_z - 2\frac{d\psi}{dz} - \frac{zRaPm}{Pr r_o}\theta = -\Lambda\left(\frac{b_\phi}{s}\right)^2 \frac{m^2}{a^2 - i\omega}u_z, \quad (3.4)$$

$$(a^2 Pm Pr^{-1} - i\omega)\theta = \frac{im\psi + zu_z}{r^3} \frac{\eta}{(1 - \eta)^2}. \quad (3.5)$$

This second-order system has boundary conditions

$$im\psi + zu_z = 0 \text{ (stress-free), } = \mp \frac{1}{2} \sqrt{\frac{Er_o}{h}} (imu_z + a^2 z\psi) \text{ (no-slip),} \quad (3.6)$$

at $z = \pm h = \pm(r_o^2 - s^2)^{1/2}$, the no-penetration/Ekman suction condition. We chose $b_\phi/s = 3\sqrt{3}z(h^2 - z^2)/2h^3$ (maximum $b_\phi/s = 1$), which is a reasonable model for the dipole fields found in our numerical simulations, so the actual field $B_\phi = \Lambda^{1/2} 3\sqrt{3}sz(h^2 - z^2)(\Omega\rho\mu\eta)^{1/2}/2h^3$. The Ekman number can be scaled out of these equations, details being given in Appendix A, and these scaled equations were solved numerically. Note that for the small E scalings to be consistent, we must have $\Lambda \sim O(E^{1/3})$, showing that even a comparatively weak magnetic field can affect the convection. This is generally consistent with the results of dynamo simulations. It comes about because at low E the rolls are thin in the azimuthal direction, and the high velocity-gradients stretch out field efficiently, generating Lorentz forces strong enough to influence the balance of Coriolis, buoyancy and viscous forces. In the Earth's core, the molecular value of the viscosity is so small that $E \sim 10^{-15}$, which would imply roll thicknesses of only tens of metres. Nonlinear effects mean that it is unlikely rolls in the core are quite as thin as that. Nevertheless, tall thin columns are suggested by low- E simulations, so linear theory may provide a useful guide to the nature of core convection. The scaled Elsasser number is then $\lambda = \Lambda E^{-1/3}$. In table 1 we show the scaled Rayleigh numbers, critical wavenumbers and frequencies in the low- E limit for cases relevant to the numerical runs in § 4. Note that increasing the magnetic field reduces the critical Rayleigh number, frequency and azimuthal wavenumber, provided the scaled Elsasser number λ is greater than unity. The reduction in critical Ra is due to the magnetic field breaking the Proudman–Taylor constraint on the rapidly rotating fluid.

λ	Pr	Pm	\hat{R}	\hat{m}	$\hat{\omega}$
0	1	1	1.15910	0.30175	0.40147
1	1	1	1.84769	0.25941	0.41451
2	1	1	1.93124	0.28074	0.07600
3	1	1	1.55264	0.22589	0.03457
4	1	1	1.24775	0.18199	0.01964
5	1	1	1.02801	0.15015	0.01263
0	10	10	2.31984	0.37092	0.45478
1	10	10	2.53093	0.36085	0.15973
3	10	10	1.58320	0.23101	0.03043
5	10	10	1.03308	0.15114	0.01215

TABLE 1. Scaled critical Rayleigh number, critical azimuthal wavenumber and frequency at the onset of convection in the low- E theory. Here λ is the scaled Elsasser number, measuring the strength of the magnetic field. The definitions of the scaled variables are given in Appendix A.

3.1. Helicity

The kinetic helicity $\mathbf{u} \cdot \boldsymbol{\zeta}$, $\boldsymbol{\zeta}$ being the vorticity, is known to be an important quantity for dynamo action (see e.g. Moffatt 1978). It is known that dynamo action can occur even if there is no helicity anywhere in the flow (Gilbert *et al.* 1988), but zero-helicity flows generally require high magnetic Reynolds numbers to become dynamos. In the rapidly rotating convection considered here, the local magnetic Reynolds number based on the convection column width is not that large, and so the first-order smoothing approximation (Moffatt 1978) is relevant. In these circumstances, we expect the helicity to be important, as found in the analysis of the dynamo mechanism occurring in rotating spherical dynamos by Olson *et al.* (1999) (although they did not consider the effect of the Lorentz force on helicity production in that paper). We would certainly advocate caution in relating dynamo action directly to the strength of the helicity, but it appears that at least in rapidly rotating flows where first-order smoothing is applicable, helicity does strongly influence the onset of dynamo action. Using the scalings (3.1), the dominant contributions to the helicity are from $u_s \zeta_s$ and $u_z \zeta_z$. In fact,

$$\mathbf{u} \cdot \boldsymbol{\zeta} = \frac{1}{s^2} \left(\frac{\partial u_z}{\partial \phi} \frac{\partial \psi}{\partial \phi} - u_z \frac{\partial^2 \psi}{\partial \phi^2} \right), \quad (3.7)$$

so both the s and z contributions to the helicity are equal. Averaged over the short azimuthal wavelength

$$H(z) = \langle \mathbf{u} \cdot \boldsymbol{\zeta} \rangle = \frac{m^2}{2s^2} (u_z \bar{\psi} + \bar{u}_z \psi). \quad (3.8)$$

In figures 1(a) and (b) we show the eigenfunctions from the Roberts–Busse equation which gives the z dependence of the solution, normalised so that the axial vorticity is unity at the boundaries. The s -dependence is less interesting, as the convection is simply concentrated near the tangent cylinder as described in Dormy *et al.* (2004). The most striking difference between figures 1(a) and (b) is the huge increase in helicity in the presence of the magnetic field. The reason for this increase is evident when the nature of the axial vorticity, $\zeta_z = a^2 \psi$, and axial velocity, u_z are considered. In figure 1(a), the axial velocity is mainly out-of-phase with the axial vorticity, thus in the normalisation used axial vorticity is primarily real (and fairly constant along the

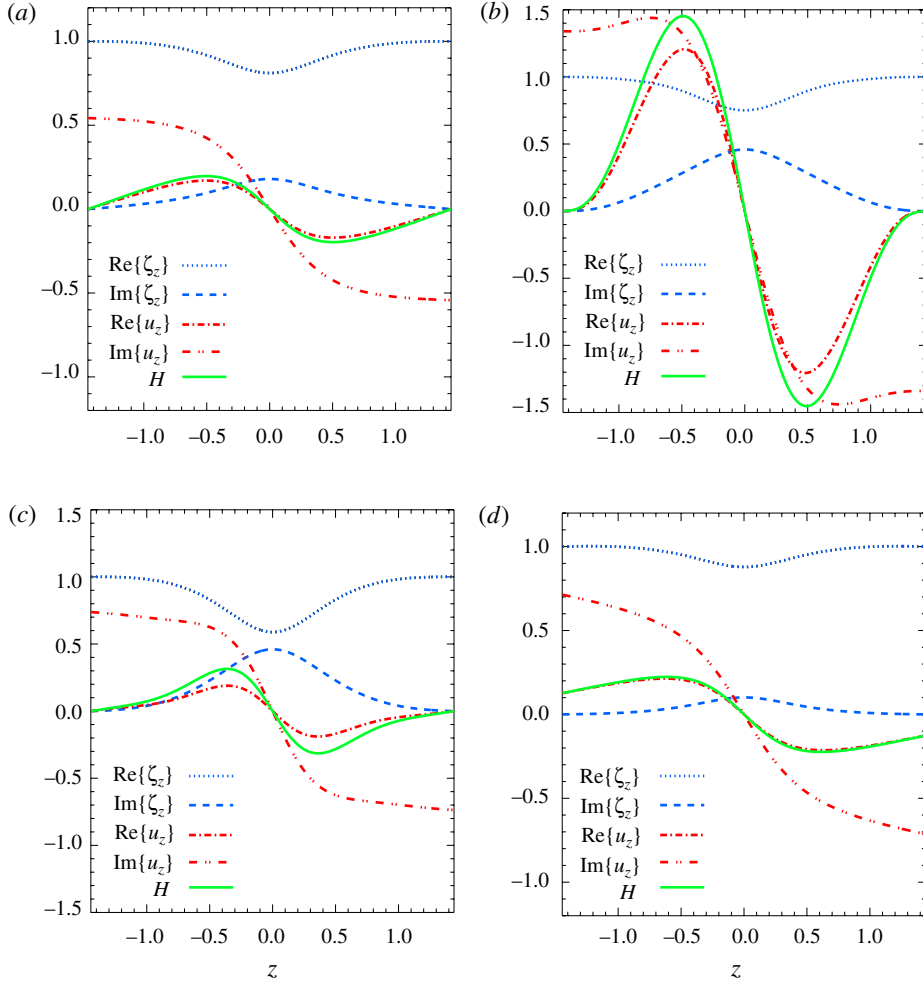


FIGURE 1. (Colour online available at journals.cambridge.org/flm) The solution of the Roberts–Busse system (3.3), (3.4), (3.5), (3.6) is shown for $Pr = Pm = 1$, together with the helicity H . Both the real and imaginary parts of ζ_z , $\text{Re}\{\zeta_z\}$ and $\text{Im}\{\zeta_z\}$, are shown, and of u_z , $\text{Re}\{u_z\}$ and $\text{Im}\{u_z\}$. (a) $\lambda = 0$, the non-magnetic solution, (b) $\lambda = 5$, solution influenced by a dipolar magnetic field. Note the massive increase in helicity when magnetic field is present. (c) $\lambda = 5$, with the quadrupolar field. Some increase in helicity over non-magnetic case is seen, but much less than with dipolar field. (d) Non-magnetic, but with the Ekman suction (no-slip) boundary condition at $E = 10^{-4}$. There is a modest increase in helicity over the stress-free case.

column), while the axial velocity is dominated by its imaginary part. Hence the mean helicity is small, because the azimuthal average is small. However, in figure 1(b), the axial vorticity is not that different, but the magnetic field ensures there is a large in-phase component to the axial velocity, and hence a much greater helicity.

The reason for this dramatic difference lies in a major change in the z -vorticity balance; see (3.3). The z -vorticity is primarily driven by buoyancy, which is strongest near the equator, where gravity acts perpendicular to the rolls and the temperature gradient is greatest. In the magnetic case, this is balanced by magnetic damping (via the Lorentz force) as well as the small viscous damping, and magnetic damping mainly

acts where the B_ϕ field is strongest, which for a dipole field is not at the equator (where it is zero), but between the equator and the boundaries. Because the driving and damping occur in different locations, stretching of the vorticity due to the background rotation is required to maintain a local balance. In both figures 1(a) and (b), the real part of the axial vorticity is roughly constant, as the term $2\mathrm{d}\psi/\mathrm{d}z$ in (3.4) is balanced only by small terms. Since it is the in-phase part of the axial velocity that provides most of the helicity, and when the field is strong the frequency is quite small, to a rough approximation we can ignore the imaginary parts of (3.3), which in the scaled form (A2) gives

$$2\frac{\mathrm{d}\hat{u}_z}{\mathrm{d}z} \approx \hat{a}^2 \hat{\zeta}_z + \lambda b_\phi^2 \hat{\zeta}_z - \frac{s^2 \hat{R} \hat{\zeta}_z}{r_o \hat{a}^2 r^3} \frac{\eta}{(1-\eta)^2}, \quad (3.9)$$

where we have used (A4) to express the buoyancy term in terms of the z -vorticity. The z -integral of this relation from the equator to the top boundary has to give a fixed value of \hat{u}_z related to $\hat{\psi}$ on the boundary through boundary condition (A5). This actually gives the real part of $\hat{u}_z = 0$ at the boundary. This integral determines the Rayleigh number required to balance the magnetic and viscous friction on the z -vorticity: the buoyancy must be sufficient to overcome both. However, the buoyancy is largest near the equator, because of the $1/r^3$ factor, whereas the magnetic friction is largest at $z \approx h/\sqrt{3}$. So (3.9) shows that $\mathrm{d}\hat{u}_z/\mathrm{d}z$ is very negative near the equator, where magnetic friction is low and buoyancy is strong. Away from the equator, where magnetic friction is large and buoyancy is quite weak, $\mathrm{d}\hat{u}_z/\mathrm{d}z$ is positive: vortex stretching generates vorticity to balance the Lorentz force. This simple argument explains the striking behaviour of the real part of the axial velocity, and hence the helicity, in figure 1(b). It follows from this argument that the axial velocity, and hence the helicity, of a quadrupolar field should be much less: in a quadrupolar field the Lorentz force peaks approximately at the same location as the buoyancy force. We expect a larger \hat{R} to balance the magnetically enhanced friction, but as the friction and the driving occur in the same place, there is no need for much vortex stretching, the right-hand side of (3.9) being roughly in balance all along the column.

In figure 1(c), the helicity and associated eigenfunctions for a quadrupolar field model are shown, with $b_\phi/s = (h^2 - z^2)/h^4$ (again maximum $b_\phi/s = 1$), and the same value of $\lambda = 5$ as in figure 1(b), so that the maximum field strength is the same in both pictures. The corresponding critical values of $\hat{R} = 3.07281$, $\hat{m} = 0.27271$ and $\hat{\omega} = 0.12741$. Note that the helicity is significantly enhanced over the non-magnetic case, but the effect is very much weaker than in the dipolar case. The helicity does increase in this quadrupolar case as the field strength increases (as it does with dipolar fields), but for the same field strength, the dipolar field produces very much more helicity. We therefore not only have a mechanism for why these dynamos are subcritical, but also have a mechanism giving a strong preference for dipolar fields over quadrupolar fields. It has long been somewhat mysterious that planetary magnetic fields are generally dipolar rather than quadrupolar (Uranus and Neptune being possible exceptions), as quadrupolar fields are quite often preferred in α -effect models and the critical dynamo numbers of dipolar and quadrupolar modes are often quite similar (Roberts 1972). Indeed, Cardin & Schaeffer (2006), who studied dynamos produced by columnar rolls driven by differential rotation (the Stewartson problem, Stewartson 1966), found that quadrupolar modes were preferred at kinematic dynamo onset, despite the geometry of the rolls being very similar to that found in this work. The essential difference, which leads to the preference for dipolar modes, is that there is an enhanced velocity

along the roll-axis, in phase with the axial vorticity. This component of the flow is much strengthened by the dipole field itself, so that once a dipolar field is established, it enhances the helicity and so tends to last for a long time. For a field reversal to occur, it is perhaps necessary to be in a strongly convecting regime, where the buoyancy force in regions away from the equator is large enough to offset the effect of the Lorentz force, so that vortex stretching in (3.9) is inhibited. In this way, strong convection can overcome the preference for dipolar solutions.

The issue of why axial dipoles are preferred to equatorial dipoles (dipolar fields with axis lying in the equatorial plane) has been discussed by Moss & Brandenburg (1995) and Tilgner (2004). Moss & Brandenburg found that strong differential rotation tended to break up large-scale non-axisymmetric fields such as equatorial dipoles by enhancing their diffusion. Tilgner notes that even in the absence of differential rotation an enhanced flow along the roll axis also favours axial dipoles over equatorial dipoles by increasing the diffusion parallel to the rotation axis. Diffusion parallel to z is more damaging to equatorial dipoles than to axisymmetric magnetic field configurations.

In figure 1(d), we repeat the figure 1(a) calculation with no imposed field, but this time use the Ekman suction condition, which corresponds to a no-slip boundary. E was chosen as 10^{-4} in this figure, and since the suction diminishes with E as $E^{1/6}$ (see (A 5) of Appendix A), a smaller E will give a lesser effect. The corresponding critical values are $\hat{R} = 1.27870$, $\hat{m} = 0.28104$ and $\hat{\omega} = 0.30109$. The suction is in phase with the axial vorticity, and so the helicity follows the axial vorticity fairly closely, and the suction increases the helicity. The maximum helicity with suction in figure 1(d) is 0.2238, as opposed to a maximum of 0.1968 with no suction, but probably more significant is that there is considerably more helicity in the Ekman layer near the upper boundary with suction. However, overall, the effect of suction on the helicity is not that great. As we see below, the effect of the boundaries in damping the nonlinearly created azimuthal flow is probably of greater significance than the effect of enhancing the helicity.

We also did some runs at $Pr = Pm = 10$ for comparison, as these values were explored by our nonlinear code. Some results are given in table 1, but the helicity graphs are not included here as they were qualitatively similar to the $Pr = Pm = 1$ case.

4. Nonlinear results

To investigate whether the results of § 3, which are based on linear studies, extend into the nonlinear regime, we performed nonlinear numerical simulations with the parameter values listed in table 2. These runs can usefully be supplemented by runs from the study of Morin & Dormy (2009), which also used the same equations (2.1), (2.2), (2.3), (2.4), (2.5) with no-slip boundary conditions.

Table 2 also gives the critical Rayleigh numbers for the onset of convection from the stationary state. For this bifurcation, small disturbances have dependence proportional to $\exp(im\phi - i\omega t)$, ϕ being the azimuthal coordinate and m the azimuthal wavenumber. The azimuthal wavenumber and frequency ω at onset are also given in table 2. Note that the asymptotic results in table 1 predict a critical value of Ra almost a factor 2 smaller even at $E = 10^{-5}$, though the predicted critical values of m and ω are closer to their numerically computed values. Dormy *et al.* (2004) noted the very slow convergence of the critical Rayleigh numbers to their asymptotic values, though the correct asymptotic values are eventually reached.

Figure 2 shows the time evolution of the magnetic energy for $E = 10^{-4}$, $Pr = Pm = 1$ and stress-free boundaries. Runs (i) ($Ra = 400$) and (ii) ($Ra = 600$) were

Case	E	Pr	Pm	Boundary conditions	Ra_{conv}	m_{crit}	ω_{crit}
1	1×10^{-4}	1	1	Stress-free	65.11	8	180.12
2	5×10^{-5}	1	1	Stress-free	73.17	10	288.62
3	10^{-5}	1	1	Stress-free	100.50	16	851.45
4	5×10^{-5}	1	1	No-slip	77.49	9	224.49
5	5×10^{-5}	10	10	Stress-free	123.77	11	382.66

TABLE 2. Critical Rayleigh number, critical azimuthal wavenumber and frequency ω at the onset of convection for the five cases studied numerically.

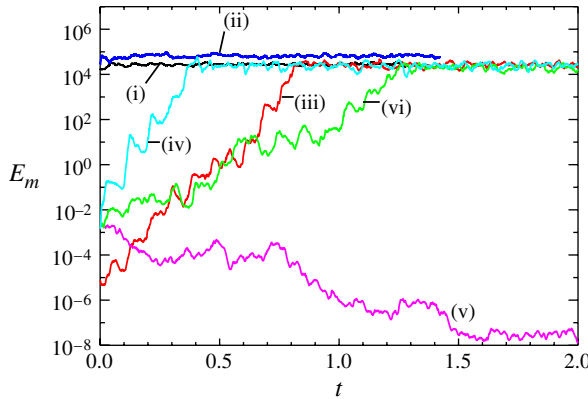


FIGURE 2. (Colour online) Evolution of magnetic energy with magnetic diffusion time for $E = 10^{-4}$, $Pr = Pm = 1$ and stress-free boundary conditions. (i) $Ra = 400$, dipole-dominated solution. (ii) $Ra = 600$, strong-field dipole-dominated solution. (iii) $Ra = 600$, initial small-field solution grows into a relatively weak quadrupolar solution. (iv) as case (iii) but with a different small initial field. (v) $Ra = 500$, an initial small field decays away. (vi) $Ra = 550$, a small initial field grows, eventually resulting in a quadrupolar field.

integrated forward in time starting from a strong-field, nonlinear dynamo solution, based on the field configuration found in the dynamo benchmark (Christensen *et al.* 2001). Here we use the term ‘strong-field’ to denote situations where the field is strong enough to significantly affect the convection. This is essentially the same definition as employed by Roberts & Soward (1992), though they were considering situations where the magnetic field could affect the critical Rayleigh number for the onset of convection, whereas here we are more interested in magnetically induced changes in the convection which affect the helicity, and hence dynamo field generation. A snapshot of the radial and azimuthal fields for the saturated dynamo is shown in figures 3(a) and (b), and a snapshot of the strong dipole field at $Ra = 600$ from a point on curve (ii) is shown in figure 3(c). Runs (iii), (iv) (v) and (vi) in figure 2 were started with a small random seed field containing all spherical harmonics up to the truncation level, too small in magnitude for the Lorentz force to have any effect on the convection initially. Since in (v) the field decays rather than grows, we deduce that $Ra > 500$ is needed for amplification of a seed magnetic field. However, at $Ra = 550$, curve (vi) shows that a dynamo does emerge from an initial, small magnetic perturbation, so the critical Rayleigh number for seed-field growth, Ra_{mag} ,

lies between 500 and 550. An established dipole field dynamo can, however, be sustained at Rayleigh numbers at least down to $Ra = 400$ as shown by curve (i). This clearly establishes the existence of subcritical dynamo action, that is to say, that a nonlinear dynamo can be maintained at values of Ra below Ra_{mag} , the critical value for seed-field growth. Note, however, that the value of Ra is still considerably larger than Ra_{conv} in table 2, though it is possible that, because a given magnetic field allows onset of convection at a lower critical Ra , dynamos could exist even at $Ra < Ra_{conv}$ as suggested by Roberts (1978) and Fautrelle & Childress (1982); see also Zhang & Gubbins (1999). Morin & Dormy (2009) found isola solutions in some parameter regimes, that is, dynamos which cannot be obtained from the growth of a small magnetic disturbance to the purely hydrodynamic convecting state, but are entirely nonlinear. For these isola solutions, a value of Ra_{mag} will not exist, though an Ra_{mag} was found for all the cases listed in table 2.

Interestingly, the magnetic field that grows from a small seed field (runs (iii), (iv) and (vi)) has a different structure from the established strongly dipolar fields of runs (i) and (ii). The starting seed field had mainly, but not exactly, a dipolar symmetry, that is, the radial and azimuthal components of the magnetic field were approximately antisymmetric about the equator. When these runs first reach saturation, they still have an approximately dipolar symmetry, an example snapshot being shown in figure 3(d). At this stage, the field is by no means dominated by the dipole component, that is, the spherical harmonic $P_1^0 \sim \cos \theta$ of the poloidal component of the magnetic field \mathcal{P} , the higher harmonics being much stronger than in the run (ii) at the same Rayleigh number. The radial field strength and magnetic energy is also considerably less than for the strong dipole case (ii). This figure 3(d) behaviour is however only a transient, though often a quite long-lived transient. After several magnetic diffusion times, the quadrupolar parity components of the field begin to grow, and eventually the field becomes entirely quadrupolar, as shown in figure 3(e). This establishes that not only is there subcriticality at $E = 10^{-4}$, there is also bistability, that is, more than one solution is stable (see also Simitev & Busse 2009; Morin & Dormy 2009).

The departure from dipolarity for the seed-field solution noted at $E = 10^{-4}$ is not observed for $E = 5 \times 10^{-5}$ and $E = 10^{-5}$: at lower Ekman numbers, the amplified seed field remains dipolar. This suggests that nonlinear inertia is present in the force balance for the seed-field state at $E = 10^{-4}$, whereas at lower E the inertial forces are weaker. Indeed, the Rossby number, $Ro = EPm^{-1}Rm$, progressively decreases for decreasing Ekman number. (The strong-field solutions found at $E = 10^{-4}$ and $Ra = 400$; $E = 5 \times 10^{-5}$ and $Ra = 400$; and $E = 10^{-5}$ and $Ra = 460$ all have volume-averaged magnetic Reynolds number Rm around or just below 100.) The strong-field solutions generally produce dipolar fields when inertia is negligible (Sreenivasan & Jones 2006a).

In figure 4(a) we see results for a lower $E = 5 \times 10^{-5}$ case also at $Pr = Pm = 1$. This establishes that growth of a seed field occurs at a Rayleigh number between 500 and 530; from runs at intermediate Rayleigh numbers we obtain $Ra_{mag} \approx 515$. In figure 4(b) we see that the nonlinear solution starting from a large-amplitude solution can be maintained at $Ra = 400$, but at $Ra = 385$ although the solution is established for nearly 0.5 diffusion times, the magnetic field does eventually fail. It seems probable that there is some critical value of $Ra = Ra_{bc}$ between 385 and 400 above which the dynamo is ‘safe’, i.e. it persists for all time, but below which the solution eventually decays, possibly after a long time. This behaviour is known as a boundary crisis of the attractor (Ott 2002), and plays a similar role to the saddle-node bifurcation found in normal hysteresis of steady solutions. We can measure the depth of subcriticality as

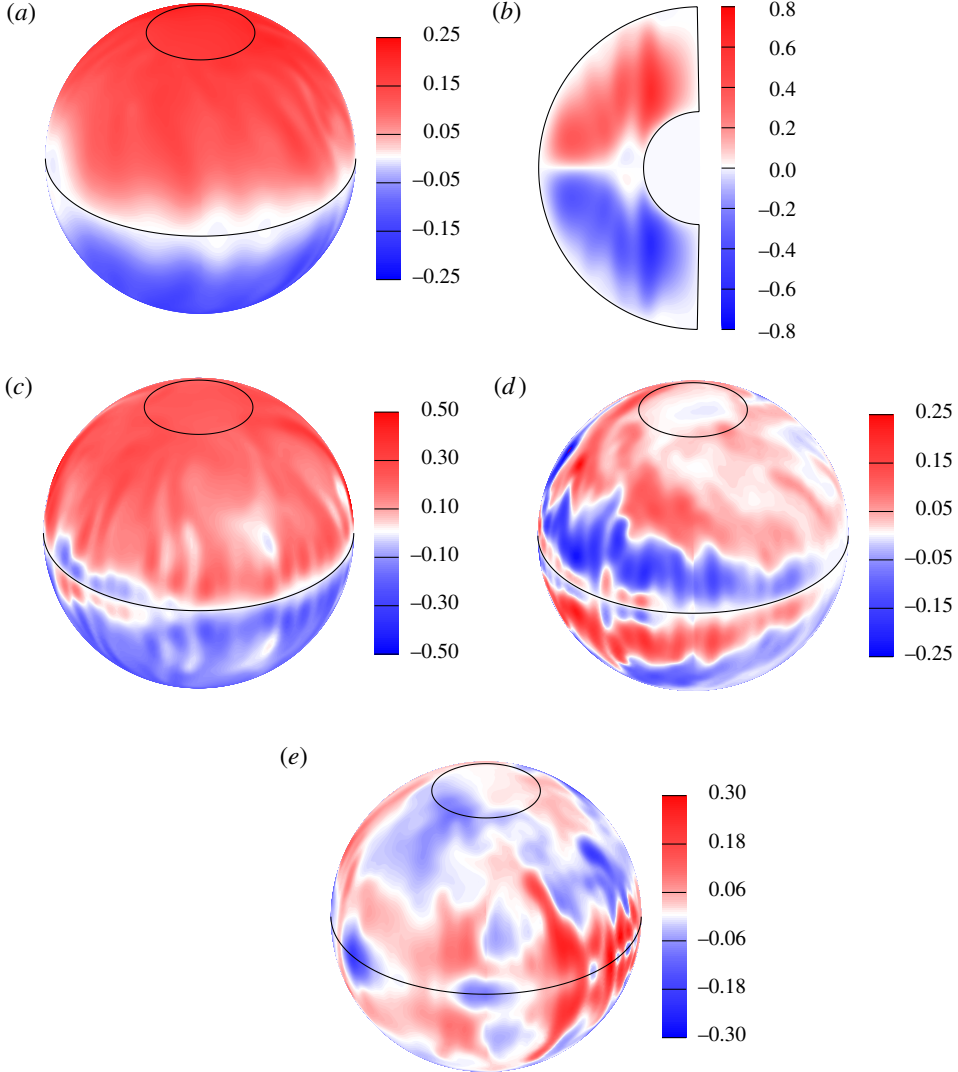


FIGURE 3. Solutions for $E = 10^{-4}$, $Pr = Pm = 1$ and stress-free boundary conditions. (a) Radial magnetic field, B_r , at the outer radius for $Ra = 400$, a saturated solution from curve (i) of figure 2. Range $(-0.159, 0.220)$. (b) Azimuthally averaged azimuthal field for the same solution. Range $(-0.620, 0.620)$. (c) Strong dipole field saturated solution at $Ra = 600$, a point on curve (ii) of figure 2. Range $(-0.273, 0.563)$. (d) Transient weak dipolar solution, from a point on curve (iv) in figure 2, at $Ra = 600$. Range $(-0.265, 0.251)$. (e) Quadrupolar solution at $Ra = 600$, from the curve (iii) run of figure 2, but after 8 magnetic diffusion times. Range $(-0.200, 0.311)$. The solid lines shown in (a), (c), (d) and (e) correspond to the equator and the latitude at which the tangent cylinder cuts the surface.

$d_{sub} = (Ra_{mag} - Ra_{bc}) / Ra_{bc}$. It would be very time-consuming to evaluate this exactly, but figure 4 suggests that at these parameter values $d_{sub} \approx 0.25$.

In figures 5(a) and (b) we find similar behaviour at lower E , suggesting that subcriticality may persist at much lower values of E , which are out of range for direct numerical simulation. A seed magnetic field grows at $Ra = 540$ but decays at

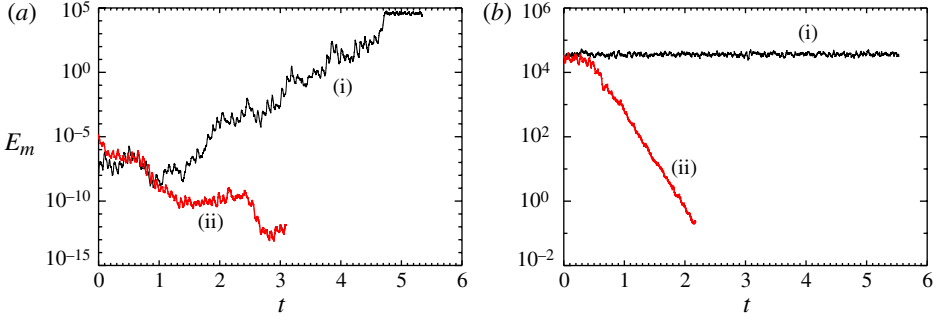


FIGURE 4. (Colour online) (a) Evolution of magnetic energy with magnetic diffusion time for $E = 5 \times 10^{-5}$ and stress-free boundary conditions from a small seed magnetic field. For case (i), $Ra = 530$, the seed field grows, but for case (ii), $Ra = 500$, the seed field decays. (b) Evolution of magnetic energy with magnetic diffusion time for $E = 5 \times 10^{-5}$ and stress-free boundary conditions from a large-amplitude solution. Case (i): $Ra = 400$, the magnetic field stays large. Case (ii): $Ra = 385$, the magnetic field solution stays large for almost half a diffusion time, but eventually falls to zero.

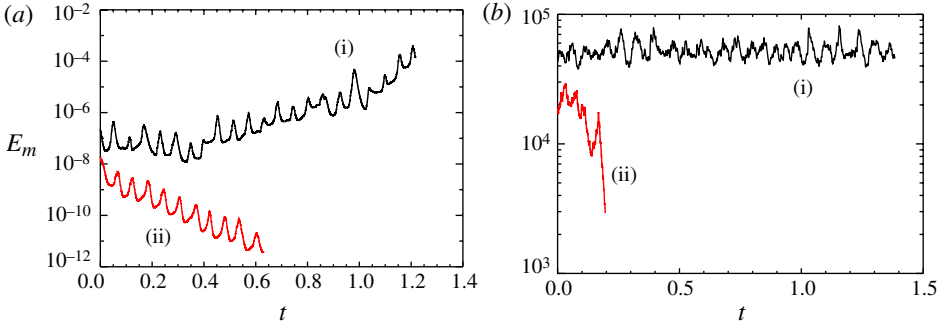


FIGURE 5. (Colour online) (a) Evolution of magnetic energy with magnetic diffusion time for $E = 10^{-5}$ and stress-free boundary conditions from a small seed magnetic field. Case (i): $Ra = 540$, the seed field grows. Case (ii): $Ra = 480$, the seed field decays. (b) Evolution of magnetic energy with magnetic diffusion time for $E = 10^{-5}$ and stress-free boundary conditions starting from a large-amplitude field solution. Case (i): $Ra = 460$, the magnetic field persists in time. Case (ii): $Ra = 420$, the magnetic field collapses.

$Ra = 480$, and interpolating the average growth rates suggests $Ra_{mag} \approx 500$. Nonlinear dipolar solutions can be sustained at much lower Ra , figure 5(b) showing a persistent solution at $Ra = 360$, though at $Ra = 340$ the dynamo failed, suggesting that in this case $Ra_{bc} \approx 350$. The depth of subcriticality d_{sub} is similar for the cases $E = 10^{-5}$ and 5×10^{-5} suggesting that the precise value is rather insensitive to the value of E , provided the boundary conditions are not changed. Calculations at lower E would be necessary to ascertain whether d_{sub} remains relatively constant or gradually decreases with decreasing Ekman number.

In figure 6 we consider no-slip boundaries rather than stress-free boundaries. As has been discussed before (Kuang & Bloxham 1997; Christensen & Wicht 2007) stress-free boundaries make a considerable difference to dynamo action. Zonal flows are stronger in stress-free cases, but also Ekman suction at the boundaries provides an additional source of helicity even when there is no Lorentz force. After careful

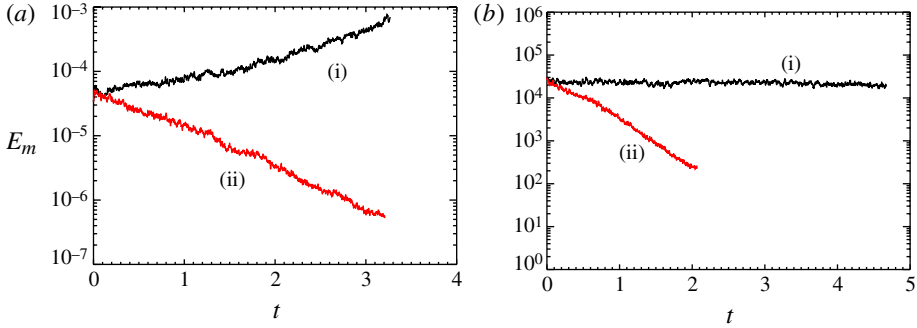


FIGURE 6. (Colour online) (a) Evolution of magnetic energy with magnetic diffusion time for $E = 5 \times 10^{-5}$ and no-slip boundary conditions from a small seed field. (i) For $Ra = 390$ the field grows, but (ii) for $Ra = 360$ the field decays. (b) Evolution of magnetic energy with magnetic diffusion time for $E = 5 \times 10^{-5}$ and no-slip boundary conditions starting from a large-amplitude solution. (i) $Ra = 360$ and the field is maintained, but in (ii) $Ra = 340$ and the magnetic field collapses.

analysis it was established that $E = 5 \times 10^{-5}$ is subcritical with no-slip boundaries, but the depth of subcriticality is much less than in the stress-free case. Figure 6(a) shows that $Ra = 390$ causes growth of a seed field but $Ra = 360$ causes the field to decay. Intermediate runs established that $Ra_{mag} \approx 377$. At $Ra = 360$, just below this, a strong-field dipolar dynamo can be maintained, and this establishes subcriticality for this case. However, the field collapses at $Ra = 340$, so the range of Ra for which nonlinear field solutions are maintained while small amplitude fields decay is comparatively small.

This no-slip case can be compared with the results of Morin & Dormy (2009), who integrated the case $E = 10^{-4}$ at $Pm = 0.67$ and $Pm = 3$. They also found subcritical bifurcation at $Pm = 0.67$, the value closest to our parameters, but found supercritical bifurcation at $Pm = 3$. We considered the case $Pr = 1$, $Pm = 3$ in our asymptotic linear magnetoconvection theory, solving equations (A 2), (A 3), (A 4), (A 5), keeping the magnetic field strength fixed at $\lambda = 5$, to compare with the case $Pr = Pm = 1$ shown in figure 1(b). At $Pm = 3$ the helicity has a similar pattern but its maximum value drops from just over 1.5 to around 1.1, so that the same magnetic field strength would lead to less helicity at $Pm = 3$ than at $Pm = 1$. This fall in helicity seems to be associated with an increase in the magnitude of the drift speed of the magnetoconvection, which at higher Pm goes westward. Additionally, their figure 6 shows that the magnetic field energy in the critical region of Ra is less at $Pm = 3$ than at $Pm = 0.67$. This means that the magnetically generated part of the helicity will be reduced at $Pm = 3$, making subcriticality less likely. The results of Morin & Dormy (2009) are therefore consistent with our argument that magnetically generated helicity helps promote subcriticality in the dynamo. It is unfortunately not easy to predict what the saturated field strength will be without doing a nonlinear simulation, and it certainly depends on parameters such as E , Pm and Pr . So subcriticality originating from magnetically driven helicity enhancement will be highly parameter-dependent, consistent with the findings of Morin & Dormy (2009).

At this point it is worth considering the case of low Pm (say, 0.1), with Pr kept fixed at unity. We might naively expect that if larger Pm reduces magnetically driven helicity enhancement, lower Pm would increase it. However, for a given E and Ra , lowering Pm would merely shut down the dynamo due to enhanced magnetic diffusion.

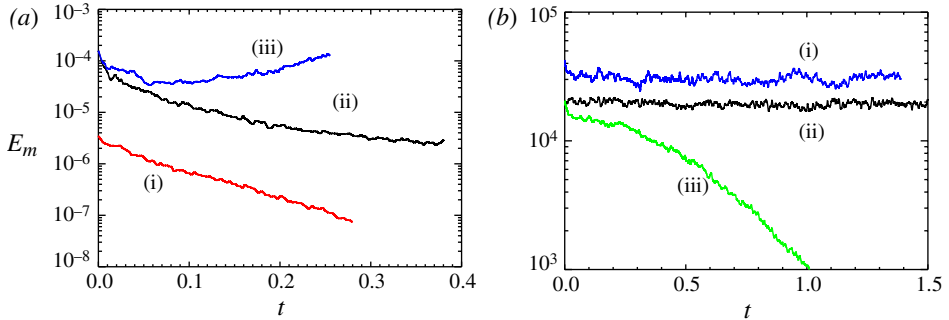


FIGURE 7. (Colour online) (a) Evolution of magnetic energy with magnetic diffusion time for $E = 5 \times 10^{-5}$, $Pr = Pm = 10$, and stress-free boundary conditions from a small seed field. (i) $Ra = 420$: not a dynamo; (ii) $Ra = 450$: near marginal for dynamo action; (iii) $Ra = 480$: a dynamo. (b) Evolution of magnetic energy with magnetic diffusion time for $E = 5 \times 10^{-5}$, $Pr = Pm = 10$ and stress-free boundary conditions starting from a large-amplitude solution. (i) $Ra = 420$, (ii) $Ra = 400$, (iii) $Ra = 360$. For $Ra = 420$ and 400 the dynamo is sustained, but for $Ra = 360$ it eventually fails.

Therefore, we must exercise caution in comparing numerical simulations at both large and small Pm with linear magnetoconvection theory. The effect of the magnetic field in enhancing helicity is best understood in a low-inertia, columnar dynamo regime.

In figure 7 we look at a solution with small nonlinear inertia, obtained by setting $Pr = Pm = 10$. Here the seed field is amplified just above $Ra = 450$, but nonlinear solutions are sustained at $Ra = 400$, so this case is again subcritical, but the depth of subcriticality is not so great as for the $Pr = Pm = 1$ solution. We shall return to this case later, while discussing figure 11.

In figure 8 we show the nature of the solution with stress-free boundaries at $E = 5 \times 10^{-5}$, $Pr = Pm = 1$. The solution from a strong-field initial state is taken at $Ra = 400$; the solution from the weak seed-field initial state is at $Ra = 500$. In figure 8(a) we show the radial magnetic field on the upper boundary, $r = r_o$. The strongly dipolar nature of the solution is apparent. There are occasional reversed flux patches near the equator, and the field where the tangent cylinder cuts the upper boundary is slightly stronger than it is at the poles, but these are the only significant departures from dipolarity. It is very unlikely that this dynamo will ever reverse its polarity. In figure 8(b) we see the radial velocity just below the upper boundary, at $r = r_i + 0.8$. The columnar nature of the convection predicted by linear theory (Jones *et al.* 2000; Dormy *et al.* 2004) is apparent at this moderately supercritical Rayleigh number. Note also that convection is still quite weak near the poles, though at higher Ra we expect much stronger polar convection (Sreenivasan & Jones 2006b; Tilgner & Busse 1997). The convection pattern is not stationary, individual rolls lasting only of the order of a turn-over time.

In figures 8(c) and (d) we compare the helicity for the strong-field solution with that for the weak-field solution. The helicity is generally approximately antisymmetric about the equator, and actually at these moderate values of Ra is quite accurately antisymmetric about the equator. We therefore show a section at $z = 0.5$ rather than the equatorial plane, where the helicity is nearly zero. This section just cuts the top of the inner sphere of radius $r_i = 0.538$. In the strong-field case, the helicity is predominantly negative, except close to the outer boundary, where there can be some weak positive helicity. In contrast, the helicity in the weak-field case is concentrated close to the

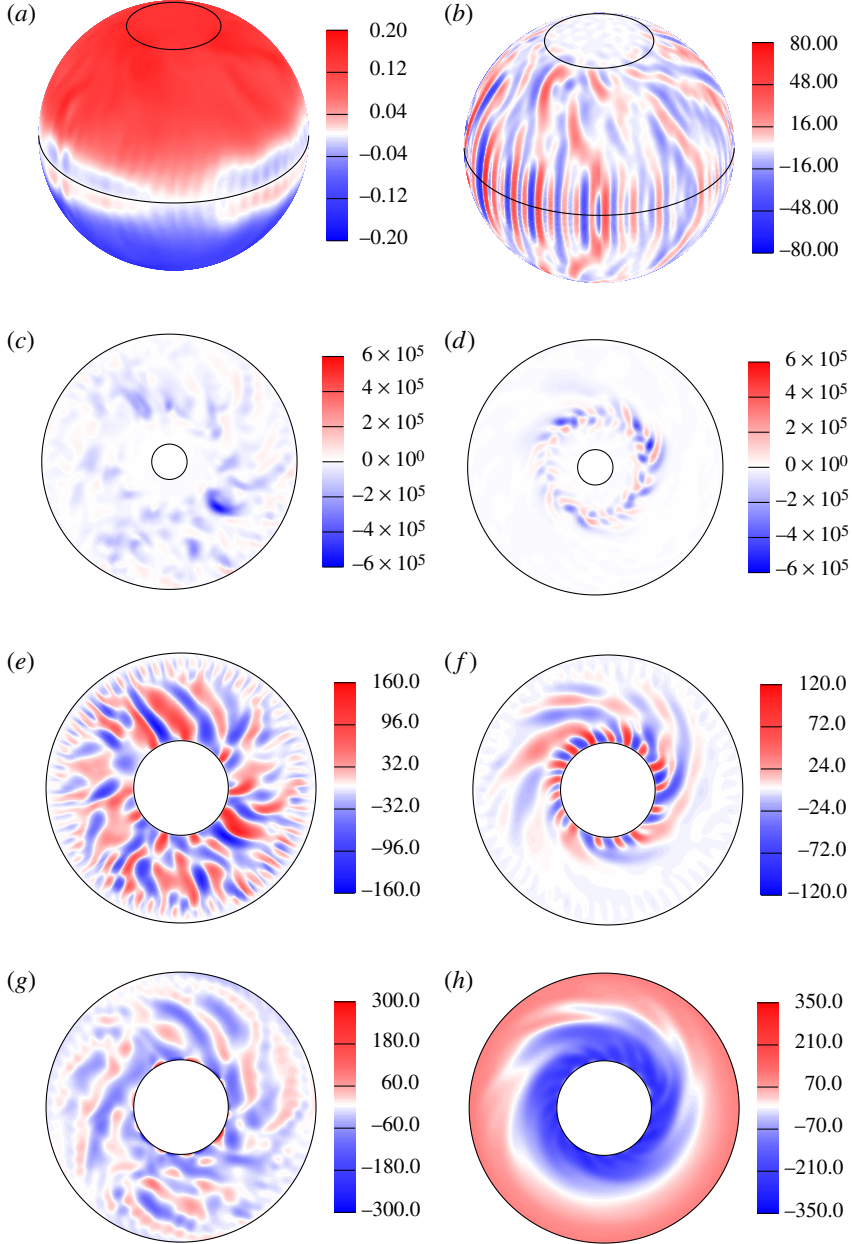


FIGURE 8. $E=5 \times 10^{-5}$, $Pr=Pm=1$, with stress-free boundaries. (a,b,c,e,g) Solutions starting from a strong field with $Ra=400$; (d,f,h) solutions starting from a weak (seed) field with $Ra=500$. (a) Radial magnetic field at the upper boundary, $r=r_o$. Range $(-0.161, 0.169)$. (b) Radial velocity at radius $r=r_i+0.8$. Range $(-61.1, 65.3)$. (c) Helicity for the strong-field solution on the plane $z=0.5$. Range $(-577000, 138000)$. (d) Helicity for the weak-field solution on the plane $z=0.5$. Range $(-530000, 209000)$. (e) Radial velocity in the equatorial plane for the strong-field solution. Range $(-154, 141)$. (f) Radial velocity in the equatorial plane for the weak-field solution. Range $(-87.3, 107)$. (g) Azimuthal velocity in the equatorial plane for the strong-field solution. Range $(-237, 262)$. (h) Azimuthal velocity in the equatorial plane for the weak-field solution. Range $(-344, 106)$.

tangent cylinder and has both positive and negative values, and a much smaller mean value. This is consistent with the results of linear magnetoconvection in § 3.

In figures 8(e) and (f) the radial velocity in the equatorial plane is shown in the strong and weak magnetic field cases respectively. The most notable feature here is that when the field is strong, convection occurs almost everywhere outside the tangent cylinder, but in the weak-field case, convection remains close to the tangent cylinder. This could be due to the magnetic field breaking the Taylor–Proudman constraint and allowing convection to occur more freely, but if this were the case we might expect a much smaller azimuthal wavenumber to dominate in the magnetic case, whereas in fact the magnetic field only reduces the dominant azimuthal wavenumber by a rather small amount. The real cause of the suppression of convection away from the tangent cylinder is the large shearing zonal flow in the weak-field case, shown in figure 8(h). This shearing flow is excited by the Reynolds stresses due to convection, but its effect is to inhibit convection where the shear is large. In contrast, when there is a strong magnetic field, the zonal flow itself is suppressed, which allows the convection to occur over a much wider region. The snapshot in figure 8(g) shows there is a significant azimuthal flow, but it is associated with the convection rolls, not the mean zonal flow. This is therefore a second nonlinear mechanism that can lead to subcritical behaviour. The magnetic field suppresses zonal flow and hence allows convection everywhere outside the tangent cylinder, thus enhancing the helicity and aiding the dynamo process. If the magnetic field gets reduced, a zonal flow builds up which switches off the convection away from the tangent cylinder, reducing the helicity and making it unlikely that the magnetic field will recover.

In figure 9 the case with E reduced to 10^{-5} is shown. Overall, the behaviour is quite similar to that at larger E . In figure 9(a) we see that the field is even more dipole-dominated, and also slightly weaker, than in figure 8(a). The convection is still columnar (as expected) in figure 9(b), and the helicity in the magnetic case is stronger and more consistently negative in the northern hemisphere slice (figure 9c) than in the weak-field case (figure 9d), as expected from the arguments in § 3. We also see that the weak-field case has a strong zonal flow (figure 9h), whose shear is suppressing convection away from the tangent cylinder (figure 9f). It might seem surprising that this low- E case, where the Reynolds stresses are weakened because the Rossby number is reduced, can still generate a large zonal flow. However, because we have stress-free and insulating boundaries, the Reynolds stresses are only opposed by weak viscous stresses, which also are reduced at lower E . However, the strong magnetic field has reduced the zonal flow in figure 9(g) very substantially, thereby allowing convection over a much larger region (figure 9e). Thus both subcritical mechanisms are at work here.

In figure 10 we return to the case $E = 5 \times 10^{-5}$, but now impose no-slip boundaries. This case had some subcritical behaviour, but much less than in the stress-free cases. The strong-field dynamo is still very dipole-dominated and columnar; see figures 10(a) and (b). The helicity mechanism is still operating, in that in the strong-field case there is more helicity and it is consistently of one sign, whereas in the weak-field case there is less helicity, and it has a few reversed helicity patches (figures 10c and d, and note the different scales). However, the second mechanism, originating from the zonal flow, is now hardly noticeable. There is no consistent zonal flow either in the weak-field case or the strong-field case – the no-slip boundary condition has much reduced the zonal flow; see figures 10(g) and (h). In consequence, the convection now occurs everywhere outside the tangent cylinder whether there is a magnetic field or not; see figures 10(e) and (f). Since the effect of the magnetic field on the helicity is

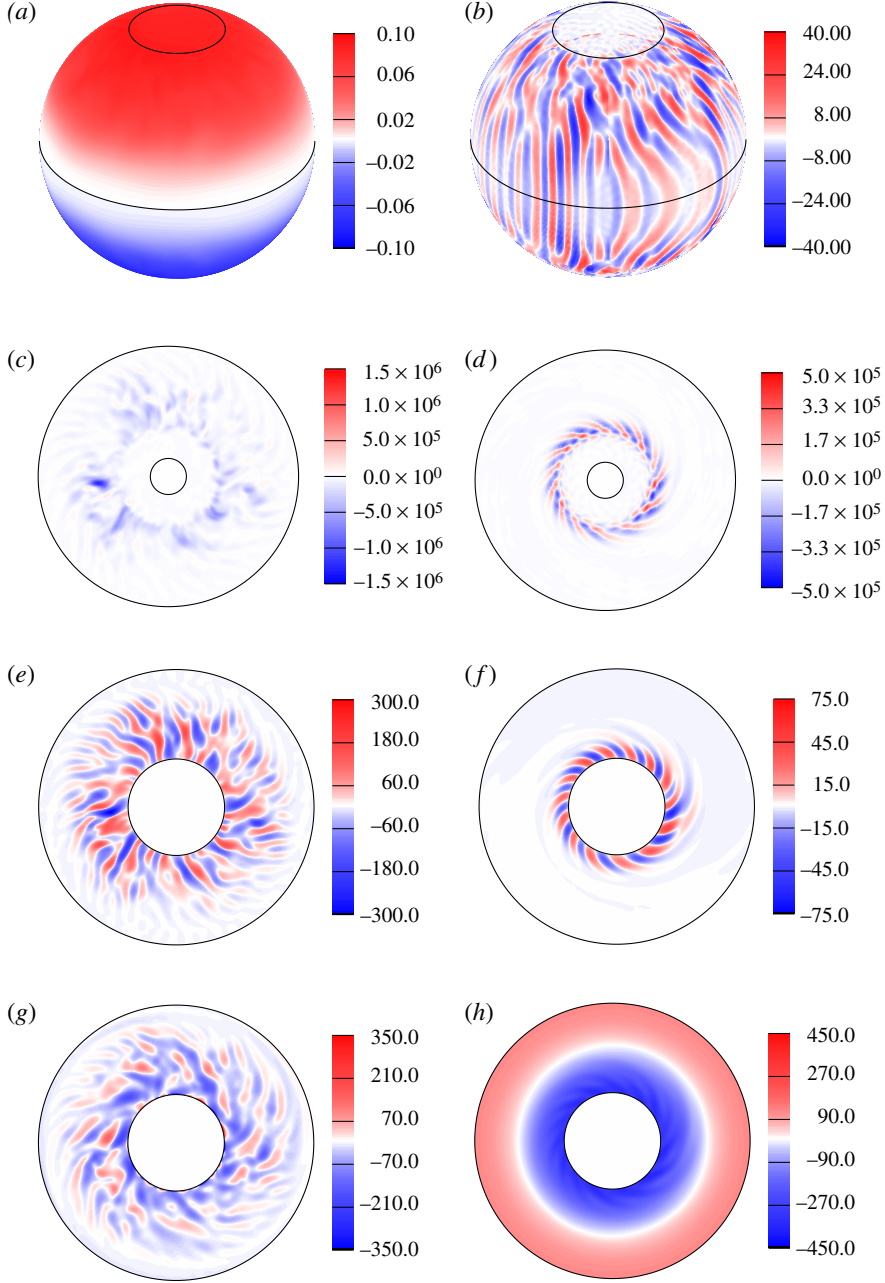


FIGURE 9. $E = 10^{-5}$, $Pr = Pm = 1$ with stress-free boundaries. (a, b, c, e, g) Solutions starting from a strong field with $Ra = 460$; (d, f, h) solutions starting from a weak field with $Ra = 480$. (a) Radial field at the upper boundary, $r = r_o$. Range $(-0.0847, 0.0904)$. (b) Radial velocity at $r = r_i + 0.8$. Range $(-37.5, 29.2)$. (c) Helicity for the strong-field solution on the plane $z = 0.5$. Range $(-1280000, 160000)$. (d) Helicity for the weak-field solution on the plane $z = 0.5$. Range $(-415000, 410000)$. (e) Radial velocity in the equatorial plane for the strong-field solution. Range $(-298, 179)$. (f) Radial velocity in the equatorial plane for the weak-field solution. Range $(-61.6, 45.2)$. (g) Azimuthal velocity in the equatorial plane for the strong-field solution. Range $(-358, 342)$. (h) Azimuthal velocity in the equatorial plane for the weak-field solution. Range $(-421, 119)$.

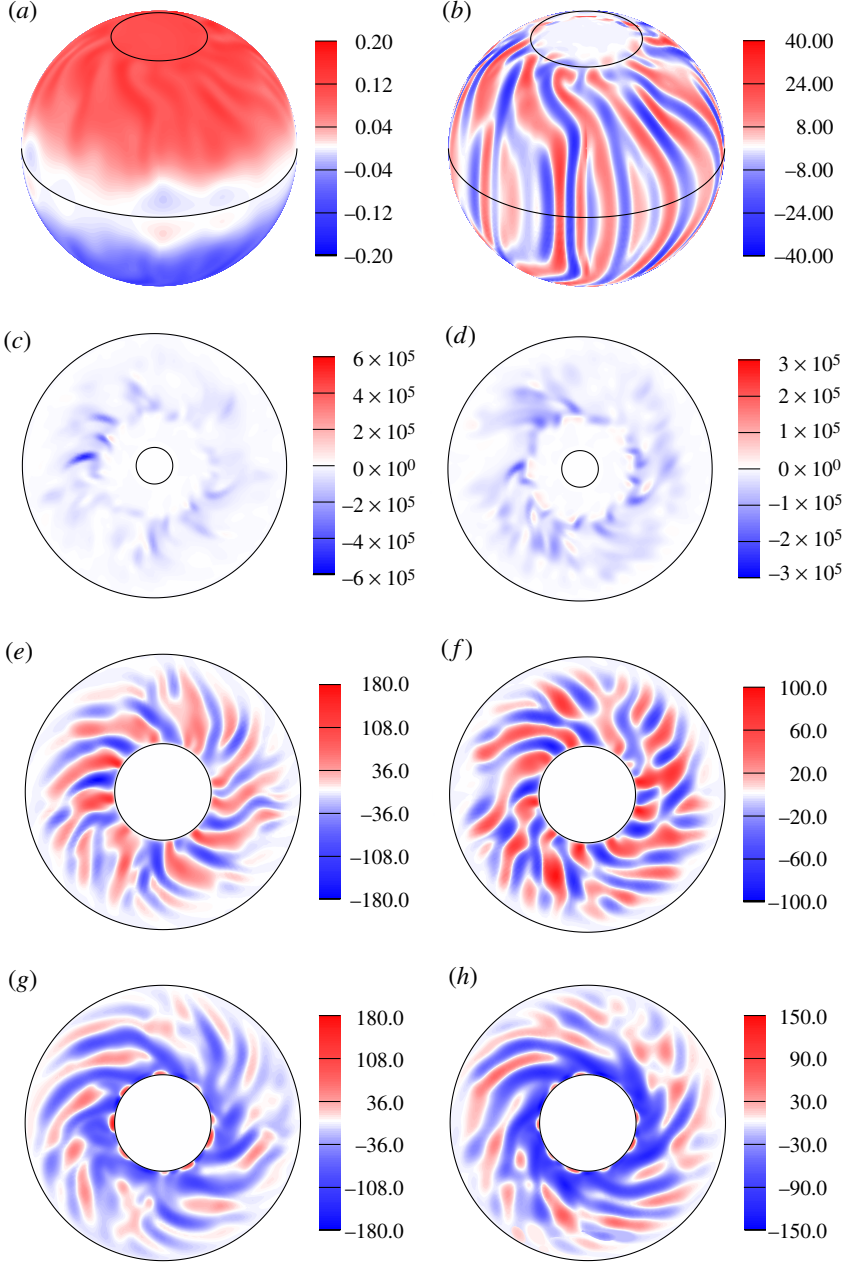


FIGURE 10. $E=5 \times 10^{-5}$, $Pr=Pm=1$ with no-slip boundaries. (a,b,c,e,g) Solutions starting from a strong field with $Ra=360$; (d,f,h) solutions starting from a weak field with $Ra=360$. (a) Radial field at $r=r_o$. Range $(-0.133, 0.177)$. (b) Radial velocity at $r=r_i + 0.8$. Range $(-33.3, 26.2)$. (c) Helicity for the strong-field solution on the plane $z=0.5$. Range $(-516000, 74900)$. (d) Helicity for the weak-field solution on the plane $z=0.5$. Range $(-193000, 40100)$. (e) Radial velocity in the equatorial plane for the strong-field solution. Range $(-176, 148)$. (f) Radial velocity in the equatorial plane for the weak-field solution. Range $(-89.5, 93.9)$. (g) Azimuthal velocity in the equatorial plane for the strong-field solution. Range $(-177, 154)$. (h) Azimuthal velocity in the equatorial plane for the weak-field solution. Range $(-148, 72.7)$.

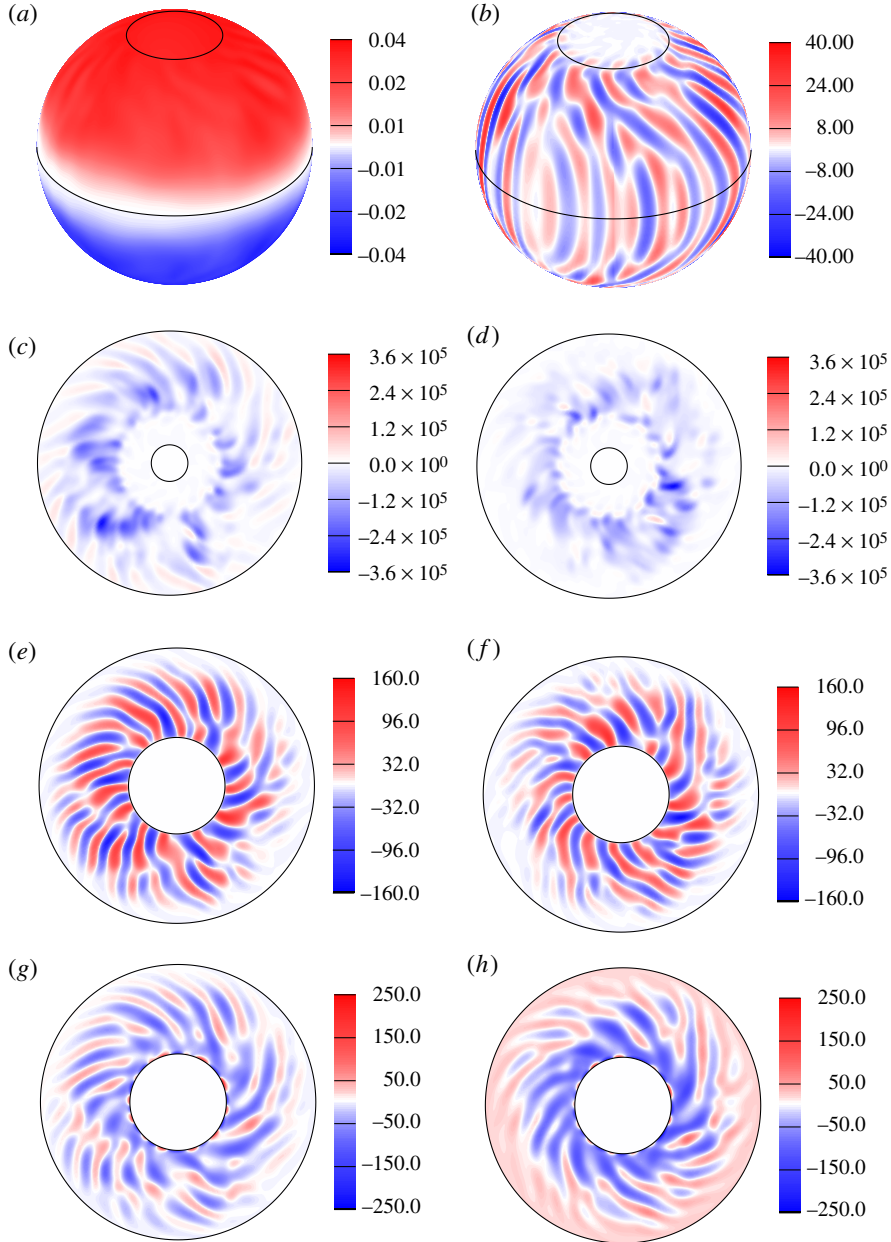


FIGURE 11. $E = 5 \times 10^{-5}$, $Pr = Pm = 10$ with stress-free boundaries. (a, b, c, e, g) Solutions starting from a strong field with $Ra = 420$; (d, f, h) solutions starting from a weak field with $Ra = 420$. (a) Radial field at $r = r_o$. Range $(-0.0359, 0.0381)$. (b) Radial velocity at $r = r_i + 0.8$. Range $(-34.5, 30.3)$. (c) Helicity for the strong-field solution on the plane $z = 0.5$. Range $(-343000, 67100)$. (d) Helicity for the weak-field solution on the plane $z = 0.5$. Range $(-350000, 65000)$. (e) Radial velocity in the equatorial plane for the strong-field solution. Range $(-139, 118)$. (f) Radial velocity in the equatorial plane for the weak-field solution. Range $(-153, 118)$. (g) Azimuthal velocity in the equatorial plane for the strong-field solution. Range $(-182, 185)$. (h) Azimuthal velocity in the equatorial plane for the weak-field solution. Range $(-242, 162)$.

still operative, it seems likely that the subcritical behaviour is due to this mechanism in this case.

In figure 11 we again consider the case $E = 5 \times 10^{-5}$, this time with stress-free boundaries, but now with $Pr = Pm = 10$, which markedly reduces the magnitude of the inertial terms in the equation of motion. As before, we still have strong dipole dominance and columnar flow (figures 11a and b), but the zonal flow is suppressed even with a weak field at the start (figure 11h), leading to convection occurring everywhere outside the tangent cylinder (figure 11f). This would explain why the weak-field helicity in figure 11(d) is more evenly distributed than in the $Pr = Pm = 1$ calculation shown earlier in figure 8(d). From figures 11(c) and (d) we note that the helicity is not enhanced much by the magnetic field, for which there is a simple explanation. The saturated field strength shown in figure 11(a) is considerably smaller than that shown in figure 8(a), and the azimuthally averaged component of B_ϕ is also more than a factor 2 less than the $Pr = Pm = 1$ run at the same value of E . The effective value of the scaled Elsasser number to be used in figure 1(b) is therefore only around $\lambda = 1$ for $Pr = Pm = 10$, whereas it is around $\lambda = 5$ with the nonlinear field strength found for $Pr = Pm = 1$. We therefore expect the effect of the magnetic field in enhancing the helicity to be much reduced in this case. The weaker saturated field for $Pr = Pm = 10$ can be traced to the higher critical Rayleigh number for convective onset, Ra_{conv} , and hence a lower value of Ra/Ra_{conv} compared to the $Pr = Pm = 1$ case at the same Ekman number (see table 2), which implies that the dynamo is less strongly driven. We recall that there is subcriticality for $Pr = Pm = 10$ (see figure 7), but the depth of subcriticality is less than for $Pr = Pm = 1$, which seems reasonable in view of the reduction in the effective value of λ .

5. Discussion and conclusions

Subcritical behaviour in rapidly rotating convection-driven dynamos appears to be quite common. For many parameter values, a nonlinear dynamo state can co-exist with a stable non-magnetic convection state. For the runs considered here, the non-magnetic convection state always became a dynamo if the Rayleigh number was raised sufficiently, so it is possible to define a depth of subcriticality that measures the range of Rayleigh number over which a nonlinear magnetic field can be maintained while the convective state is stable to small magnetic perturbations. Morin & Dormy (2009) found that at much higher Rayleigh numbers, the non-magnetic convection solution could restabilise, leading to a finite range of Rayleigh number for which a dynamo starting from a seed field is possible. We have not explored this possibility here, but instead have concentrated on trying to understand the physical mechanisms that are leading to subcritical behaviour.

The first mechanism we have established is that the magnetic field enhances the helicity of the convective flow under rapid background rotation. This is achieved by the Lorentz force enhancing the flow along the axis of the convection columns. This effect is mainly found with fields of dipolar symmetry, and so dipolar fields can more strongly enhance helicity than quadrupolar fields. Since helicity helps to sustain the dynamo against magnetic diffusion, this effect gives a strong preference towards dipolar fields over quadrupolar fields, or over fields with a more complicated morphology. This may help to explain why dipolar fields are so frequently found in dynamo simulations when inertial effects in the equation of motion are negligible. Since inertial effects are believed to be of little importance in planetary dynamos, this may indeed be the reason why many planetary magnetic fields are dipolar. This

first mechanism also leads to subcritical behaviour, because if the magnetic field is removed, the helicity is reduced and may be insufficient to allow a small seed field to grow. On the other hand, if the magnetic field is imposed as an initial condition, the helicity generated can be sufficient to maintain it against diffusion for ever.

This first mechanism can be studied by means of the linear theory of magnetoconvection, as shown in § 3. Magnetoconvection studies such as this can suggest plausible mechanisms, as here, but they do suffer from the disadvantage that they assume a magnetic field with a simple uniform structure. In a dynamo simulation, the magnetic field usually has in addition to the mean field a complicated small-scale structure, caused by flux being expelled from eddies. It is therefore not always easy to make a quantitative comparison of magnetoconvection results with dynamo simulations. Nevertheless, the predicted effect of an enhanced and more coherent helicity in the presence of a dipolar field fits the results from the simulations rather well.

The second mechanism for subcriticality we have discovered is connected with the presence of a zonal flow, that is, an azimuthally averaged u_ϕ . Strong shearing zonal flows exist with stress-free boundaries and no magnetic field, and such a zonal flow suppresses convection and hence helicity in a large fraction of the core. So if no magnetic field is present, it is hard to get one started. On the other hand, if a strong field is present *ab initio*, the shearing zonal flow is eliminated and there is plenty of convection and helicity to sustain the field. This second mechanism is evident in figures 8 and 9, but it is probably less robust than our first mechanism. Since no-slip boundaries tend to reduce the zonal flow, there is less opportunity for helicity suppression with these boundary conditions. Also, at larger Pr and Pm the driving of the zonal flow by Reynolds stresses is reduced.

Since our helicity mechanism suggests a reason why dipolar fields are preferred, natural questions are why dipolar fields are not found in all dynamo simulations, and how can the dynamo reverse its polarity? The appearance of non-dipolar dynamos is strongly associated with the importance of the inertial terms in the equation of motion (Sreenivasan & Jones 2006a), that is, the Rossby number not being sufficiently small, or more precisely the local Rossby number defined as $U/\ell\Omega$ where ℓ is the dominant length scale of the convection (Olson & Christensen 2006). When nonlinear inertia is important, the columnar structure tends to break down, and so the whole picture of helicity giving rise to an α^2 -type dynamo ceases to be valid. Without well-defined columns, the arguments given in § 3 become meaningless, because the actual flow is nothing like the flow at onset. As noted in § 3.1, it is possible that departures from dipolar symmetry, leading to field reversals, occur when the magnetically enhanced columnar flow structure breaks down when the convective driving is very strong. At large Pr and Pm , when inertial forces are negligible, dipole-dominated dynamos would persist to a large Ra , but eventually we would expect small-scale components of the flow to disrupt the columnar structure, and hence destroy the systematic helicity correlation which seems to produce the large-scale magnetic field.

Appendix A. The low- E scaling of the linear equations

The equations (3.3), (3.4), (3.5), which are valid in the limit of small E , can be rescaled to eliminate the Ekman number itself.

The appropriate asymptotic scalings for the variables are (Jones *et al.* 2000, 2003)

$$\left. \begin{aligned} Ra &= E^{-1/3} \hat{R}, & \omega &= E^{-2/3} \hat{\omega}, & m &= E^{-1/3} \hat{m}, & k &= E^{-1/3} \hat{k}, \\ a &= E^{-1/3} \hat{a}, & \theta &= E^{2/3} \hat{\theta}, & \psi &= E^{1/3} \hat{\psi}, & u_z &= \hat{u}_z, & \Lambda &= E^{1/3} \hat{\lambda}. \end{aligned} \right\} \quad (\text{A } 1)$$

The resulting equations are

$$(\hat{a}^2 - i\hat{\omega}Pm^{-1})\hat{a}^2\hat{\psi} - 2\frac{d\hat{u}_z}{dz} + \frac{i\hat{m}\hat{R}Pm}{r_oPr}\hat{\theta} = -\lambda\left(\frac{b_\phi}{s}\right)^2\frac{\hat{m}^2\hat{a}^2}{\hat{a}^2 - i\hat{\omega}}\hat{\psi}, \quad (\text{A } 2)$$

$$(\hat{a}^2 - i\hat{\omega}Pm^{-1})\hat{u}_z - 2\frac{d\hat{\psi}}{dz} - \frac{z\hat{R}Pm}{r_oPr}\hat{\theta} = -\lambda\left(\frac{b_\phi}{s}\right)^2\frac{\hat{m}^2}{\hat{a}^2 - i\hat{\omega}}\hat{u}_z, \quad (\text{A } 3)$$

$$(\hat{a}^2PmPr^{-1} - i\hat{\omega})\hat{\theta} = \frac{i\hat{m}\hat{\psi} + z\hat{u}_z}{r^3}\frac{\eta}{(1-\eta)^2}. \quad (\text{A } 4)$$

The boundary conditions are

$$i\hat{m}\hat{\psi} + z\hat{u}_z = 0 \text{ (stress-free)}, \quad = \mp \frac{1}{2}E^{1/6}\sqrt{\frac{r_o}{h}}(i\hat{m}\hat{u}_z + \hat{a}^2z\hat{\psi}) \text{ (no-slip)}, \quad (\text{A } 5)$$

at $z = \pm h = \pm(r_o^2 - s^2)^{1/2}$, the no penetration or Ekman suction condition. Note that the Ekman suction is still (weakly) dependent on E , even in the low- E limit. At extremely low E , as may be found in the Earth's core, Ekman suction will be small, but in numerical models, where very low E is impossible for computational reasons, Ekman suction is significant when there are no-slip boundaries. For the dipole model $b_\phi/s = 3\sqrt{3}z(h^2 - z^2)/2h^3$, which has a maximum of unity, and for the quadrupole model $b_\phi/s = (h^2 - z^2)^2/h^4$, which has maximum unity on the equator. The actual dipolar field $B_\phi = E^{1/6}\lambda^{1/2}3\sqrt{3}sz(h^2 - z^2)(\Omega\rho\mu\eta)^{1/2}/2h^3$. The equations (A 2), (A 3), (A 4), (A 5) were solved by a finite-difference method to give the results shown in table 1, and the helicity distributions in figure 1.

For comparison with the work of Dormy *et al.* (2004), which used a different scaling of the equations from the scaling used here, the following relations may be useful,

$$\left. \begin{aligned} \hat{\omega}_P &= (1 - r_i/r_o)^{2/3} 2^{2/3} Pm \omega_D, & \hat{a}_P &= 2^{1/3} (1 - r_i/r_o)^{1/3} a_D, \\ \hat{m} &= 2^{1/3} (1 - r_i/r_o)^{-2/3} m_D, & \hat{R}_P &= 2^{4/3} (1 - r_i/r_o)^{1/3} r_i^{-1} \hat{R}_D, \end{aligned} \right\} \quad (\text{A } 6)$$

where the subscript P denotes the present values, and subscript D those quoted in Dormy *et al.* (2004). Thus at $\lambda = 0, Pr = Pm = 1$, for the present differential heating Dormy *et al.* found (equation (5.1) in their paper) $\hat{R}_D = 0.285933$, $\omega_D = 0.337014$ and $m_D = 0.179715$. Using (A 6) to convert these values to our units we obtain $\hat{R}_P = 1.15910$, $\hat{\omega}_P = 0.401430$, $\hat{m} = 0.301753$, in excellent agreement with the values found in table 1.

REFERENCES

- AUBERT, J. & WICHT, J. 2004 Axial and equatorial dipolar dynamo models with implications for planetary magnetic fields. *Earth Planet. Sci. Lett.* **221**, 409–419.
- BUSSE, F. H. 1970 Thermal instabilities in rapidly rotating systems. *J. Fluid Mech.* **44**, 441–460.
- BUSSE, F. H. 1976 Generation of planetary magnetism by convection. *Phys. Earth Planet. Inter.* **12**, 350–358.
- BUSSE, F. H. & CARRIGAN, C. R. 1976 Laboratory simulation of thermal convection in rotating planets and stars. *Science* **191**, 81–83.
- BUSSE, F. H. & SIMITEV, R. D. 2006 Parameter dependences of convection-driven dynamos in rotating spherical fluid shells. *Geophys. Astrophys. Fluid Dyn.* **100**, 341–361.
- CARDIN, P. & SCHAEFFER, N. 2006 Quasi-geostrophic kinematic dynamos at low magnetic Prandtl number. *Earth Planet. Sci. Lett.* **245**, 595–604.
- CHRISTENSEN, U. R. *et al.* 2001 A numerical dynamo benchmark. *Phys. Earth Planet. Inter.* **128**, 25–34.

- CHRISTENSEN, U. R. & WICHT, J. 2007 Numerical dynamo simulations. In *Treatise on Geophysics* (volume editor P. Olson, series editor G. Schubert), vol. 8, pp. 245–282. Elsevier.
- CLUNE, T. C., ELLIOT, J. R., MIESCH, M. S., TOOMRE, J. & GLATZMAIER, G. A. 1999 Computational aspects of a code to study rotating turbulent convection in spherical shells. *Parallel Comput.* **25**, 361–380.
- DORMY, E., SOWARD, A. M., JONES, C. A., JAULT, D. & CARDIN, P. 2004 The onset of thermal convection in rotating spherical shells. *J. Fluid Mech.* **501**, 43–70.
- FAUTRELLE, Y. & CHILDRESS, S. 1982 Convective dynamos with intermediate and strong fields. *Geophys. Astrophys. Fluid Dyn.* **22**, 235–279.
- GILBERT, A. D., FRISCH, U. & POUQUET, A. 1988 Helicity is unnecessary for α effect dynamos, but it helps. *Geophys. Astrophys. Fluid Dyn.* **42**, 151–161.
- JONES, C. A. 2007 Thermal and compositional convection in the outer core. In *Treatise on Geophysics* (volume editor P. Olson, series editor G. Schubert), vol. 8, pp. 131–185. Elsevier.
- JONES, C. A., MUSSA, A. I. & WORLAND, S. J. 2003 Magnetoconvection in a rapidly rotating sphere: the weak-field case. *Proc. R. Soc. Lond. A* **459**, 773–797.
- JONES, C. A., SOWARD, A. M. & MUSSA, A. I. 2000 The onset of thermal convection in a rapidly rotating sphere. *J. Fluid Mech.* **405**, 157–179.
- KONO, M. & ROBERTS, P. H. 2002 Recent geodynamo simulations and observations of the geomagnetic field. *Rev. Geophys.* **40**, 1013.
- KUANG, W. & BLOXHAM, J. 1997 An Earth-like numerical dynamo model. *Nature* **389**, 371–374.
- KUANG, W., JIANG, W. & WANG, T. 2008 Sudden termination of Martian dynamo?: implications from subcritical dynamo simulations. *Geophys. Res. Lett.* **35**, L14204.
- LILLIS, R. J., FREY, H. V., MANGA, M., MITCHELL, D. L., LIN, R. P., ACUÑA, M. H. & BOUGHER, S. W. 2008 An improved crustal magnetic map of Mars from electron reflectometry: highland volcano magmatic history and the end of the Martian dynamo. *Icarus* **194**, 575–596.
- MOFFATT, H. K. 1978 *Magnetic Field Generation in Electrically Conducting Fluids*, p. 343. Cambridge University Press.
- MORIN, V. & DORMY, E. 2009 The dynamo bifurcation in rotating spherical shells. *Intl J. Mod. Phys. B* **23**, 5467–5482.
- MOSS, D. & BRANDENBURG, A. 1995 The generation of nonaxisymmetric magnetic fields in the giant planets. *Geophys. Astrophys. Fluid Dyn.* **80**, 229–240.
- OLSON, P. & CHRISTENSEN, U. R. 2006 Dipole moment scaling for convection-driven planetary dynamos. *Earth Planet. Sci. Lett.* **250**, 561–571.
- OLSON, P., CHRISTENSEN, U. & GLATZMAIER, G. A. 1999 Numerical modelling of the geodynamo: mechanisms of field generation and equilibration. *J. Geophys. Res.* **104**, 10383–10404.
- OTT, E. 2002 *Chaos in Dynamical Systems*. Cambridge University Press.
- ROBERTS, P. H. 1968 On the thermal instability of a rotating fluid sphere containing heat sources. *Phil. Trans. R. Soc. Lond. A* **263**, 93–117.
- ROBERTS, G. O. 1970 Spatially periodic dynamos. *Phil. Trans. R. Soc. Lond. A* **266**, 535–558.
- ROBERTS, P. H. 1972 Kinematic dynamo models. *Phil. Trans. R. Soc. Lond. A* **272**, 663–698.
- ROBERTS, P. H. 1978 Magneto-convection in a rapidly rotating fluid. In *Rotating Fluids in Geophysics* (ed. P. H. Roberts & A. M. Soward), pp. 421–435. Academic.
- ROBERTS, P. H. & SOWARD, A. M. 1992 Dynamo theory. *Annu. Rev. Fluid Mech.* **24**, 459–512.
- SIMITEV, R. D. & BUSSE, F. H. 2009 Bistability and hysteresis of dipolar dynamos generated by turbulent convection in rotating spherical shells. *Europhys. Lett.* **85**, Art. No. 19001.
- SREENIVASAN, B. & JONES, C. A. 2006a The role of inertia in the evolution of spherical dynamos. *Geophys. J. Intl* **164**, 467–476.
- SREENIVASAN, B. & JONES, C. A. 2006b Azimuthal winds, convection and dynamo action in the polar regions of planetary cores. *Geophys. Astrophys. Fluid Dyn.* **100**, 319–339.
- SREENIVASAN, B. 2009 On dynamo action produced by boundary thermal coupling. *Phys. Earth Planet. Inter.* **177**, 130–138.
- STEWARTSON, K. 1966 On almost rigid rotations. *J. Fluid Mech.* **26**, 131–144.
- TILGNER, A. 2004 Small-scale kinematic dynamos: beyond the α -effect. *Geophys. Astrophys. Fluid Dyn.* **98**, 225–234.

- TILGNER, A. & BUSSE, F. H. 1997 Finite-amplitude convection in rotating fluid shells. *J. Fluid Mech.* **332**, 359–376.
- ZELDOVICH, Y. B. 1957 The magnetic field in the two-dimensional motion of a conducting turbulent fluid. *Sov. Phys. JETP* **4**, 460–462.
- ZHANG, K. 1992 Spiralling columnar convection in rapidly rotating spherical fluid shells. *J. Fluid Mech.* **236**, 535–556.
- ZHANG, K. & GUBBINS, D. 1999 Scale disparities and magnetohydrodynamics in the Earth’s core. *Phil. Trans R. Soc. Lond. A* **358**, 899–920.